Electronic Supplementary Material (ESI) for Journal of Materials Chemistry A.
This journal is © The Royal Society of Chemistry 2024

A Strategy to Build High-performance Thick Electrodes for Lithium-ion Batteries with Enhanced Compressive Modulus and Regulated Tortuosity in Phase-inversion Processing

Yifan Zhang[1], Yaohong Xiao[2], Lei Chen[2], Shan Hu[1,*]

[1] Department of Mechanical Engineering, Iowa State University, 2529 Union Drive, Ames, IA 50010, USA

[2] Department of Mechanical Engineering, University of Michigan-Dearborn, 4901 Evergreen Road, Dearborn, MI 48128, USA

* Corresponding author: shanhu@iastate.edu

Change of Thermodynamics with introduction of ethanol to non-solvent

The Gibbs free energy of mixing ($^{\Delta G_m}$) for a ternary system with nonsolvent (1), solvent (2) and polymer (3) can be expressed as[1]:

$$\frac{\Delta G_m}{RT} = n_1 ln\phi_1 + n_2 ln\phi_2 + n_3 ln\phi_3 + g_{12} u_2 n_1 \phi_2 + \chi_{13} n_1 \phi_3 + \chi_{23} n_2 \phi_3 \#(S1)$$

in which R is ideal gas constant, T is the temperature, n_i and ϕ_i represent number of molecules and volume fraction of component i in the system, respectively, g_{12}, $\chi_{13}$and χ_{23} stand for interaction parameters of solvent-nonsolvent, nonsolvent-polymer and solvent-polymer, respectively. The interaction parameter g_{12}can be calculated as[2]:

$$g_{12} = \frac{V_1}{RT}(\delta_1 - \delta_2)^2 \#(S2)$$

V and δ represent volume fraction and solubility parameter, respectively. Based on the solubility parameters of ethanol, water and NMP recorded in literature[3,4], the value of g_{12} decreases when adding ethanol into the non-solvent, indicating better mixability between the nonsolvent and solvent.

According to calculation of $^{\Delta G_m}$, decrease of g_{12} will mean less nonsolvent is needed for the phase inversion therefore favors the instantaneous de-mixing of the ternary system[1,5] and the generation of finger-like channels[6]. Whereas high g_{12} will mean more nonsolvent is needed for the phase inversion therefore favors the delayed de-mixing of the ternary system[1,5] and the generation of sponge-like structure with cellular pores[1]. Additionally, the decrease of g_{12} induces higher concentration of polymer in the polymer-rich region[1], which explains the enhanced compressive modulus of electrode fabricated by using water-ethanol mixture as nonsolvent compared to those prepared with pure water as nonsolvent. In summary, the addition of ethanol in the non-solvent favors the instantaneous de-mixing to form finger-like structures inside the electrode and aids the improvement of the mechanical properties.

Calculation of lithium-ion diffusion coefficient ($^{D_{Li^+}}$) from electrochemical measurements

Nyquist plots were acquired by electrochemical impedance spectroscopy (EIS) tests. According to the semi-infinite diffusion model, the Warburg impedance (Z_w) is expressed as[7]:

$$Z_w = \sigma\omega^{-1/2}(1-j)\#(S3)$$

where σ and ω represent the Warburg coefficient and the angular frequency, respectively. The Warburg coefficient (σ) can be obtained by calculating the linearly fitted data of Z_w versus the inverse square root of the angular frequency ($\omega^{-1/2}$) in the low-frequency region. The Warburg coefficient σ is related to the lithium-ion diffusion coefficient (D_{Li^+}) as:

$$\sigma = \frac{RT}{\sqrt{2}An^2F^2CD_{Li^+}^{1/2}}\#(S4)$$

where R is ideal gas constant (8.314 J mol^{-1} K^{-1}), T is the temperature, A is the area of electrode surface, n is the number of electrons involved in the redox reaction, F is Faraday constant (96485 C mol^{-1}), C is the molar concentration of lithium ions. Therefore, D_{Li^+} of each electrode is calculated using S4 with σ from EIS data and all the constants.

Galvanostatic intermittent titration technique (GITT) was implemented to investigate the kinetics of the as-prepared free-standing electrodes by half-cell configuration (lithium metal as counter electrode). In the measurement, the duration of charge and discharge pulse was regulated as 30 minutes at C-rate of 0.1 C, then the cell was allowed 1 hour of relaxation before the next current pulse started. From the GITT profile, diffusion coefficient of lithium-ions D_{Li^+} can be calculated with the following equation[8]:

$$D_{Li^+} = \frac{4}{\pi\tau}\left(\frac{nV_m}{A}\right)^2\left(\frac{\Delta E_s}{\Delta E_\tau}\right)^2\#(S5)$$

in which τ is the time of current pulse, n is the moles of active material, V_m is the molar volume, A is the area of the electrode, ΔE_s is the change of steady-state voltage, and ΔE_τ is the voltage change during charge/discharge pulse. The acquisition of data from GITT profile is demonstrated in Fig. S6.

Cyclic voltammetry (CV) was performed at scan rate of 0.1, 0.15, 0.2 and 0.25 mV/s in the voltage window of 2.5 to 4.2 V for all electrode samples with half-cell setup (lithium metal as the counter electrode). The peak current (i_p) and scan rate (ν) follows the relation based on Randles-Sevcik equation[9]:

$$i_p = 2.69\times10^5 n^{\frac{3}{2}}AD_{Li^+}^{\frac{1}{2}}C_{Li^+}\nu^{\frac{1}{2}}\#(S6)$$

where i_p is the peak current, n is the number of electrons transferred in the redox reaction, A is the area of electrode, D_{Li^+} is the diffusion coefficient of lithium-ion, C_{Li^+} is the change of concentration of lithium-ion, ν is the scan rate. As plotted in Fig. 4d and 4e, peak current can be linearly fitted with square root of scan rate ($\nu^{1/2}$). In Randles-Sevcik equation, parameters of n, A

and C_{Li^+} are constants, lithium-ion diffusion coefficient of each LFP electrode is obtained from the slope of fitted line in both anodic and cathodic region. In this case for LFP cathode, the value of n, A and C_{Li^+} are 1, 1.27 cm^2 and 2.28 mol/cm^3, respectively.

Estimation of porosity of electrode

The porosity of electrode (ε) is estimated by the ratio of the volume of solid materials (V_m) to the actual volume of electrode (V_e), which is expressed as: $\varepsilon = 1 - V_m/V_e$. The as-prepared electrode includes LFP, PVDF and acetylene black (AB), and the volume of solid materials in the electrode is: $V_m = \frac{m_{LFP}}{\rho_{LFP}} + \frac{m_{PVDF}}{\rho_{PVDF}} + \frac{m_{AB}}{\rho_{AB}}$, in which m and ρ represent mass and density of each material. The theoretical density of LFP, PVDF and AB used in the calculation are 3.6, 1.78 and 1.95 g/cm^3, respectively. The volume of actual electrode is calculated as: $V_e = A \times t_e$, in which A stands for the area of electrode and t_e is the thickness of electrode measured through SEM images, respectively.

Tortuosity measurement

The tortuosity of the LFP electrodes was measured by DC-polarization method with symmetric cells. In the symmetric cell, the LFP electrode prepared by phase-inversion method was sandwiched between two layers of Celgard 2400 polymer separators and lithium chips as illustrated in the inset demonstration of Fig. 5a. After assembly, the cell rested for 2 hours to be wetted completely by the electrolyte (1 M $LiPF_6$ in EC: EMC = 3:7). The cell was charged at current of 10 μA for 2 hours to generate a concentration gradient followed by relaxing until dU/dt < 0.1 mV/h. The cell voltage is expressed by equation (S7) in the following[10]:

$$U(t) = \frac{i_p L}{\sigma} + \left(\frac{\sigma_{el}}{\sigma}\right)\left(\frac{i_p L}{\sigma_{ion}}\right)\left[1 - \frac{8}{\pi^2}\exp\left(-\frac{t}{t^{\delta}}\right)\right] \#(S7)$$

in which i_p and L indicates the polarization current and thickness of electrode, respectively, σ, σ_{el} and σ_{ion} represent the overall, electronic and ionic conductivity, respectively, t^{δ} is the characteristic relaxation time. Based on this equation, the plot of $\ln|U(t) - U(t = \infty)|$ versus time was produced to determine the characteristic relaxation time by fitting the linear region of the plot. Finally, lithium-ion diffusivity (D) was calculated based on equation (S8),

$$t^{\delta} = \frac{L^2}{\pi^2 D} \#(S8)$$

in which L is the thickness of electrode. With the obtained effective diffusivity of lithium-ion, tortuosity of LFP electrode can be calculated by equation (S9):

$$\tau = \frac{\varepsilon D_0}{D_{eff}} \#(S9)$$

The same method was applied to measure the intrinsic diffusivity D_0. Instead of free-standing LFP electrode, one piece of 1.63-mm thick PTFE O-ring (McMaster) was used to separate the two

layers of Celgard 2400 separator and lithium chips on each side. The tortuosity of each LFP electrode was calculated by equation (S9), in which porosity of each electrode was determined individually by Archimedes method.

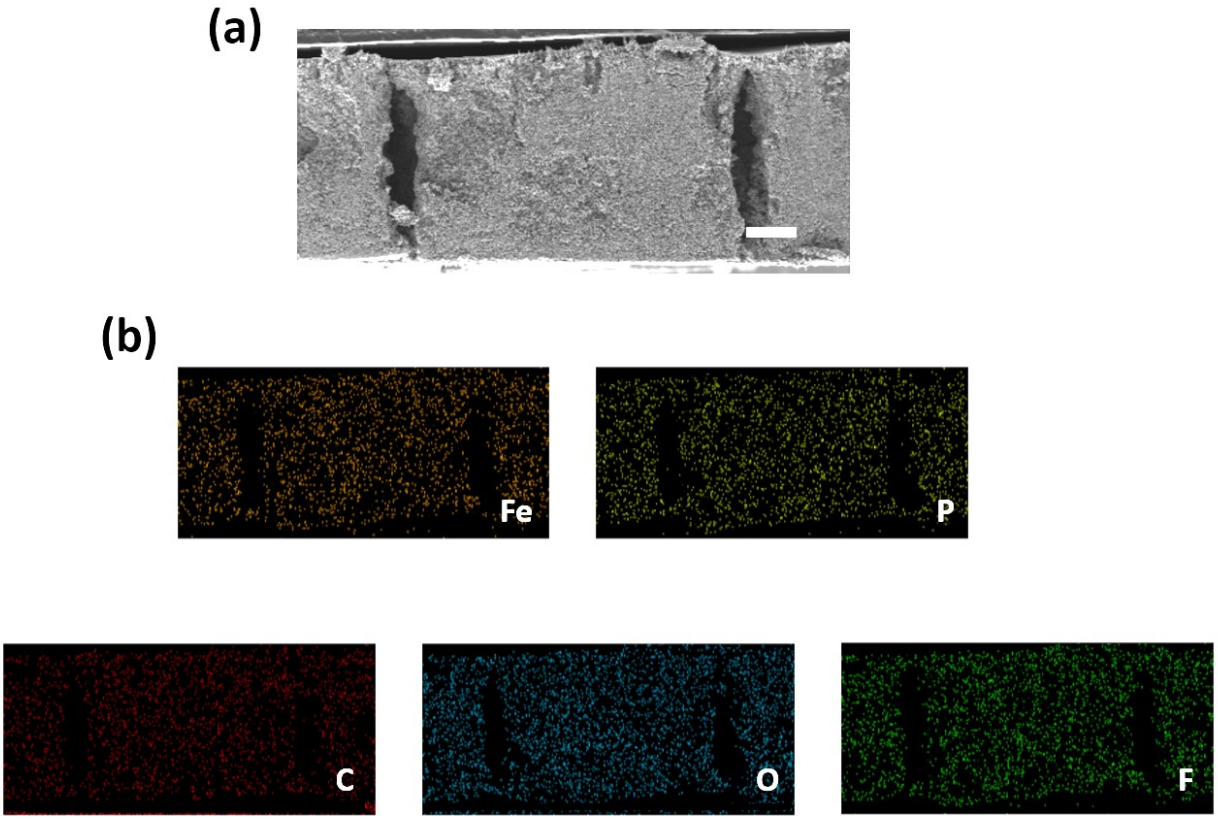

Fig. S1. SEM images of cross-sectional area of (a) WE31-40 electrode (scale bar: 200 μm) with its (b) EDS mappings.

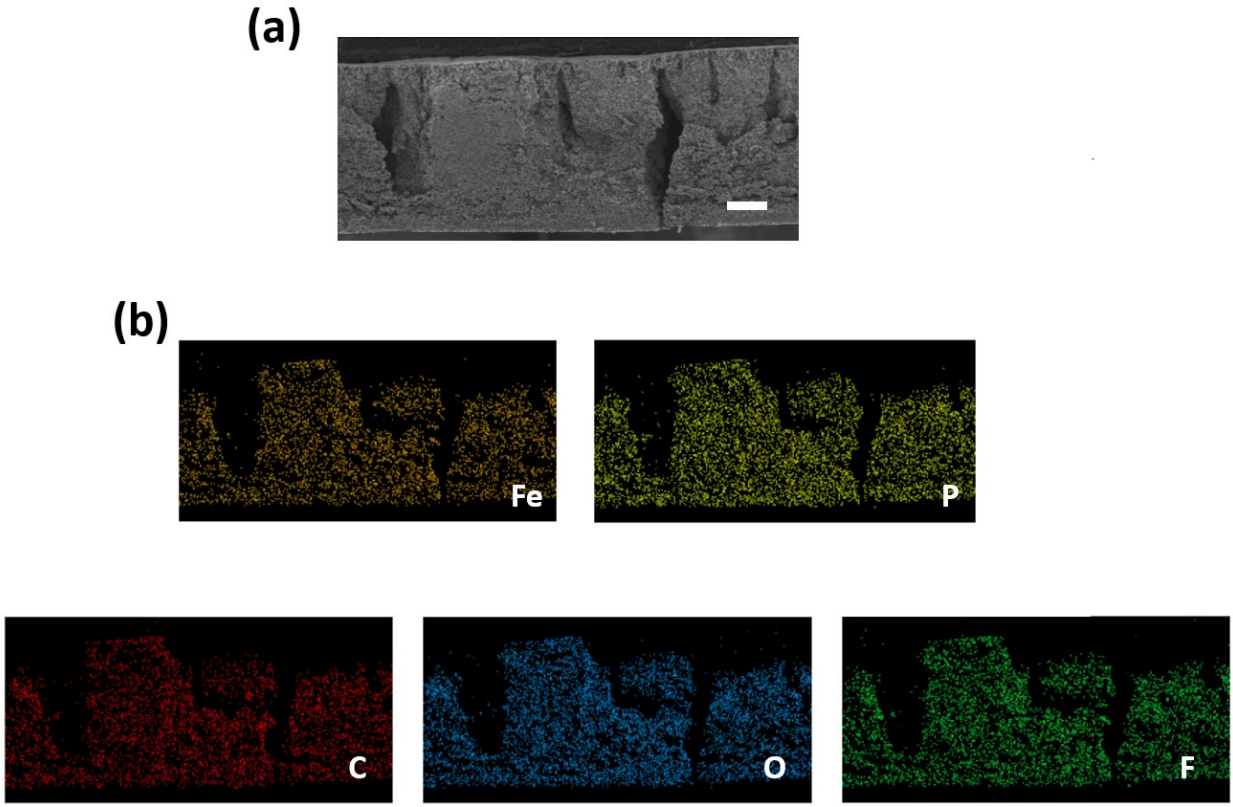

Fig. S2. SEM images of cross-sectional area of (a) WE41-40 electrode (scale bar: 200 μm) with its (b) EDS mappings.

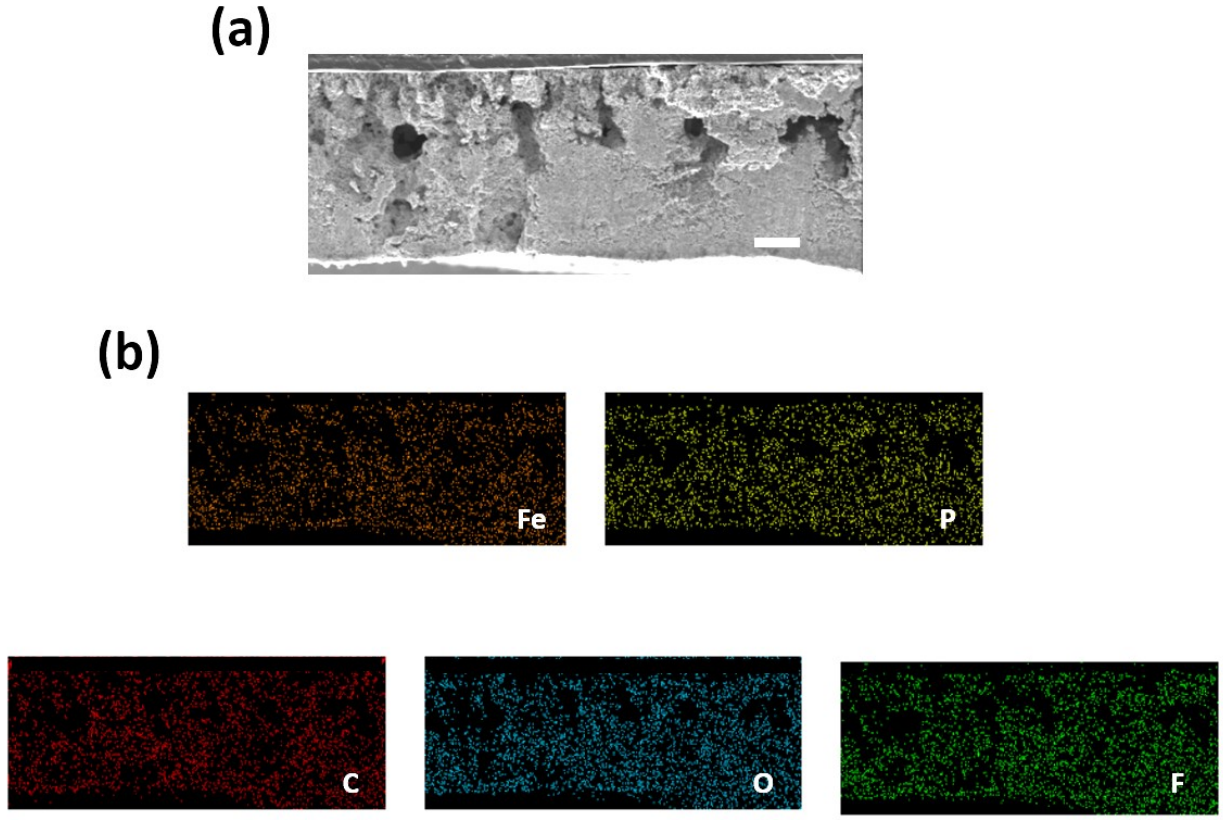

Fig. S3. SEM images of cross-sectional area of (a) WE51-40 electrode (scale bar: 200 μm) with its (b) EDS mappings.

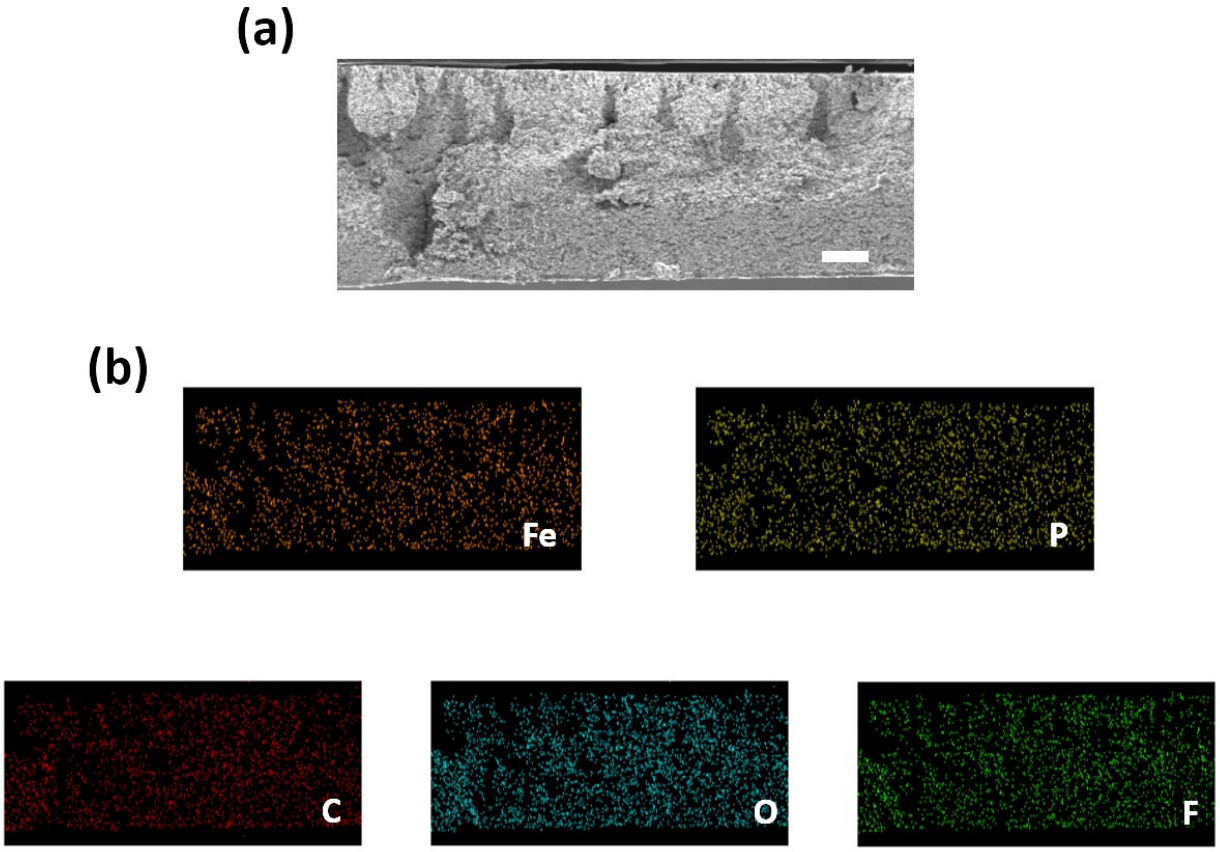

Fig. S4. SEM images of cross-sectional area of (a) DIW-40 electrode (scale bar: 200 μm) with its (b) EDS mappings.

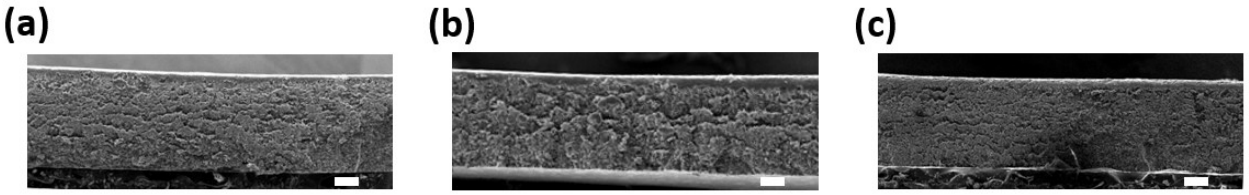

Fig. S5. SEM images of cross-sectional area of (a) WE21-40, (b) WE11-40 and (c) WE12-40 electrodes (scale bar: 200 μm).

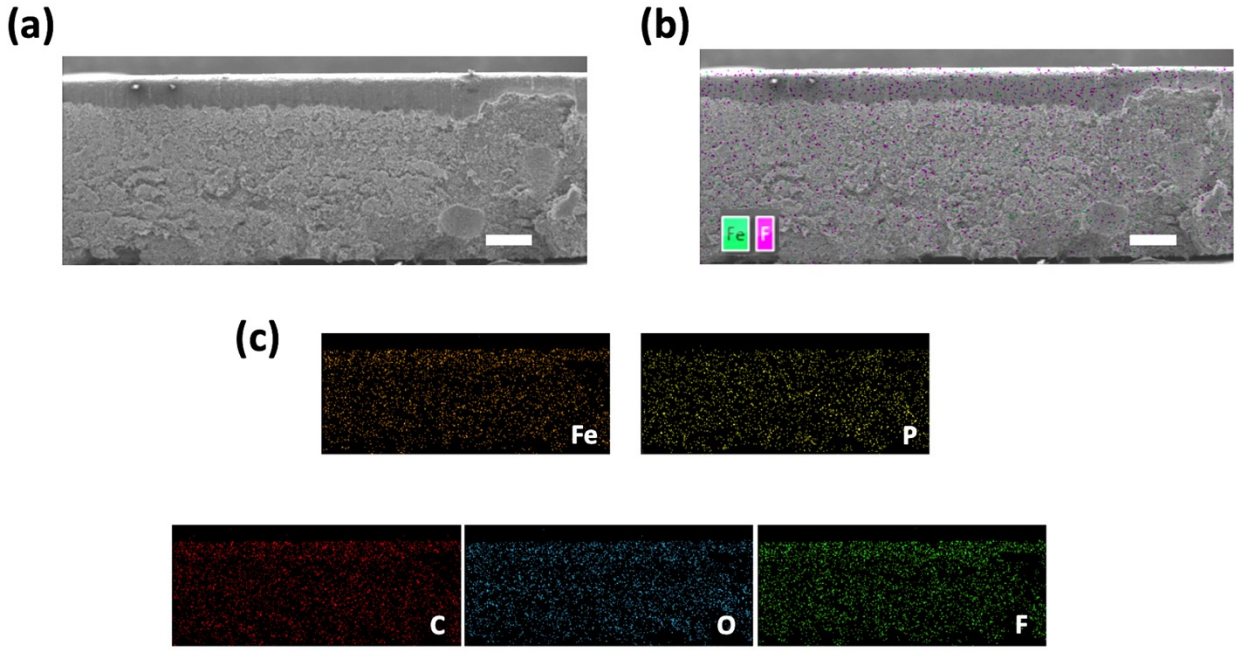

Fig. S6. (a) SEM images of cross-sectional area of WE21-40 electrodes (scale bar: 200 μm); (b) EDS mapping of element iron and fluorine (scale bar: 200 μm); (c) Complete EDS mappings of each element in WE21-40 electrode.

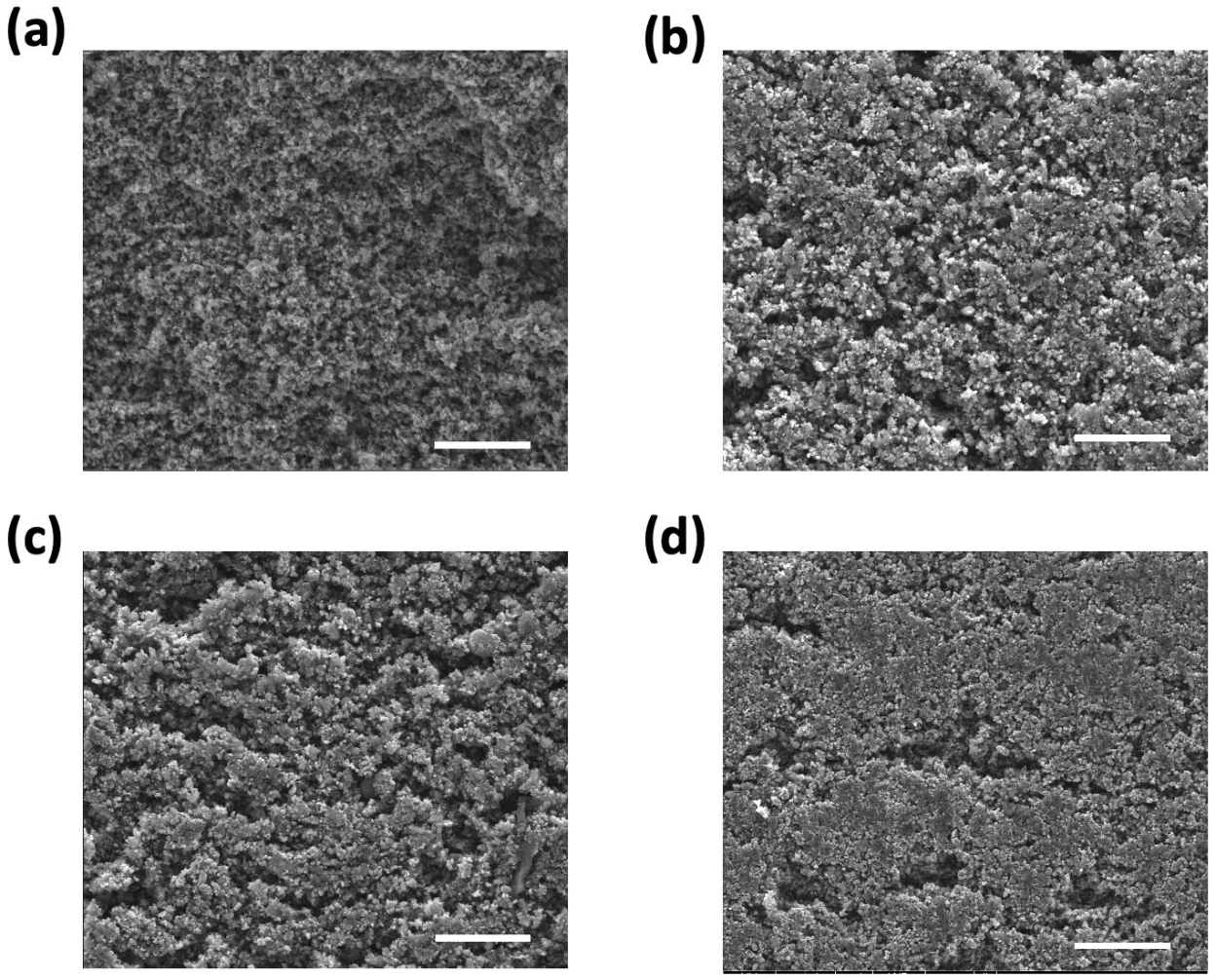

Fig. S7. SEM images of polymer-rich region in (a) WE31-40, (b) WE41-40, (c) WE51-40 and (d) DIW-40 electrodes at high magnification (scale bar: 25 μm).

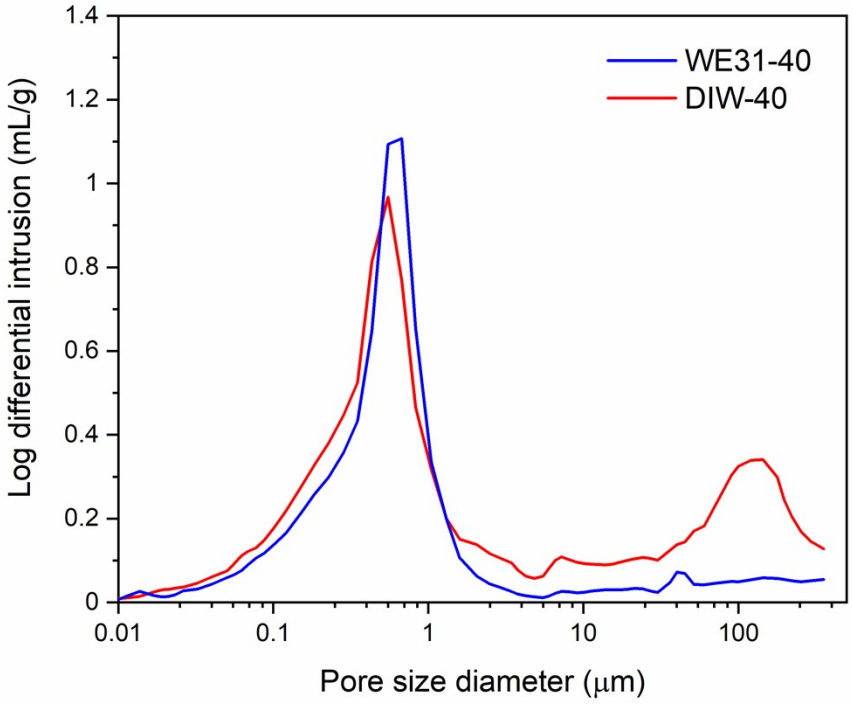

Fig. S8. Pore size distribution of WE31-40 and DIW-40 electrodes.

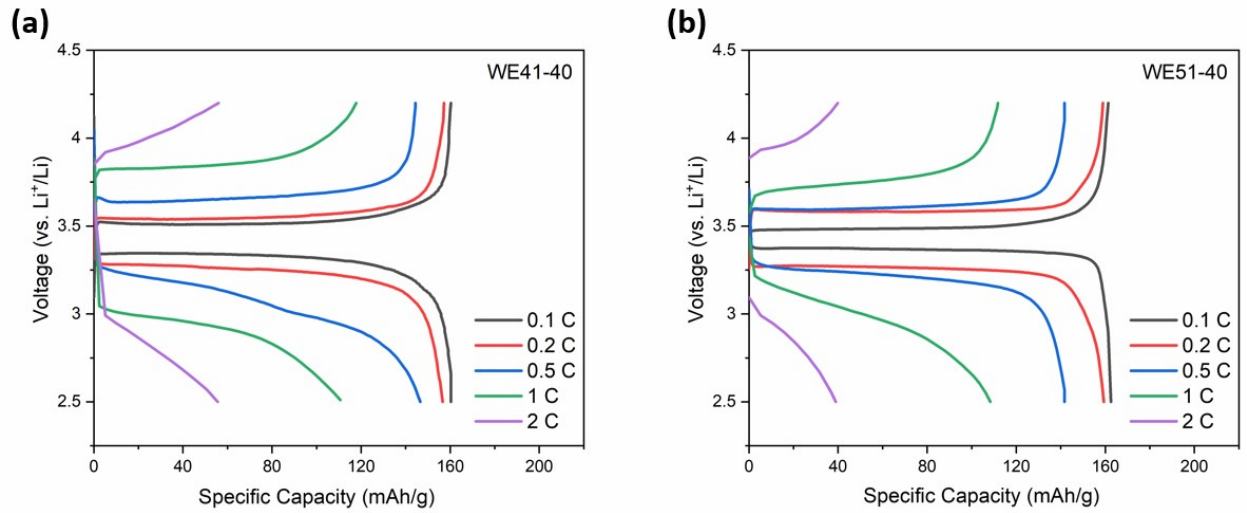

Fig. S9. Voltage profile of (a) WE41-40 and (b) WE51-40 electrodes during charge and discharge at various C-rates.

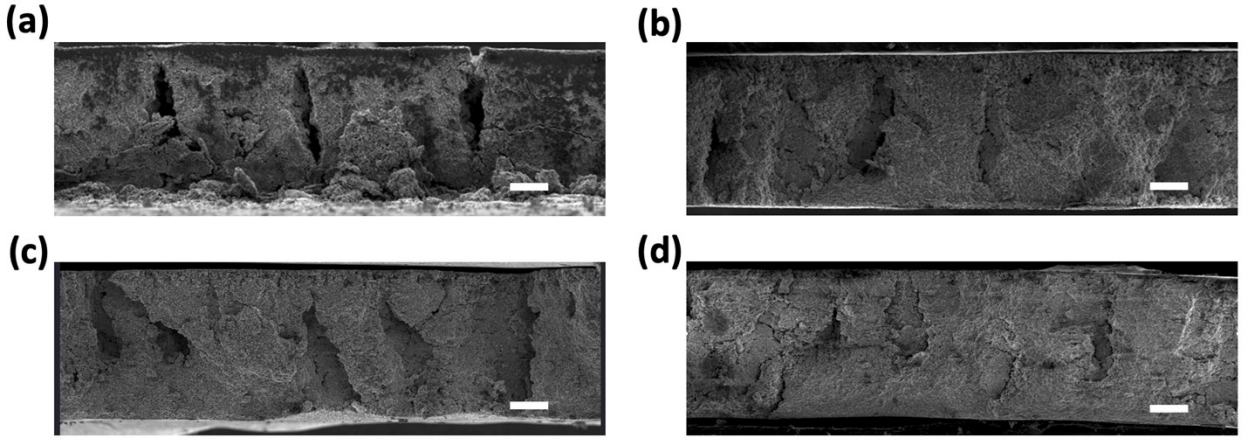

Fig. S10. SEM images of cross-sectional area of (a) WE31-40, (b) WE41-40, (c) WE51-40 and (d) DIW-40 electrodes after long-term cycling for 200 cycles at 0.5 C (scale bar: 200 μm).

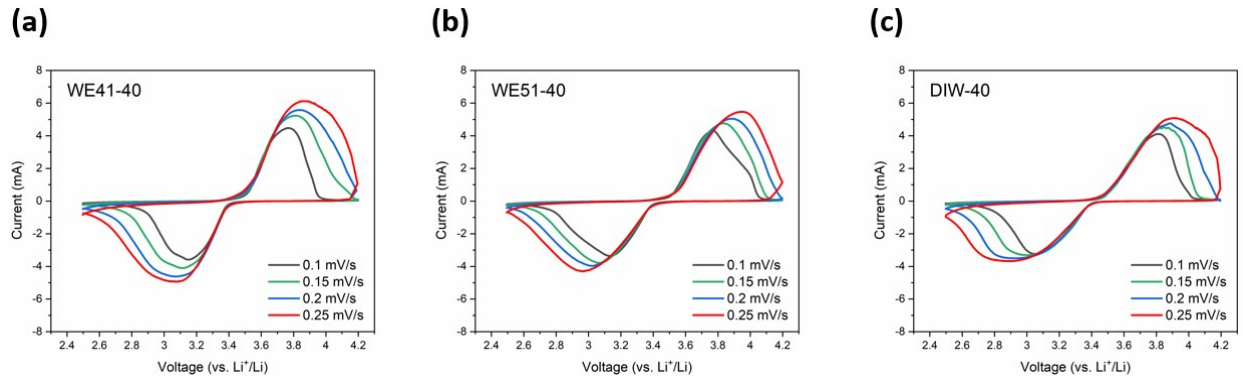

Fig. S11. Cyclic voltammograms of (a) WE41-40, (b) WE51-40 and (c) DIW-40 electrodes at scan rate of 0.1, 0.15, 0.2 and 0.25 mV/s, respectively.

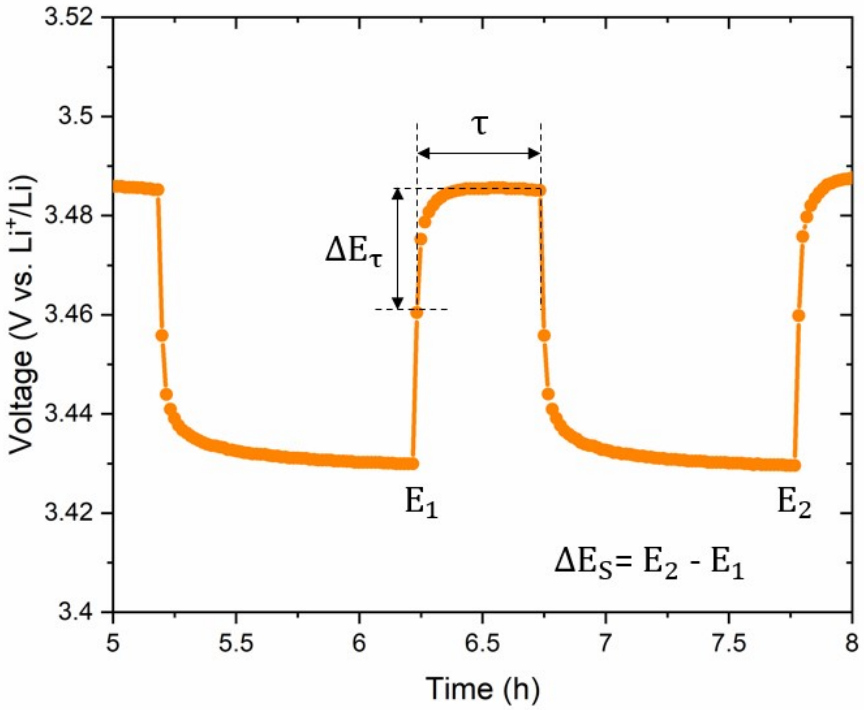

Fig. S12. Example of GITT profile and illustration of parameters involved in the calculation for lithium-ion diffusion.

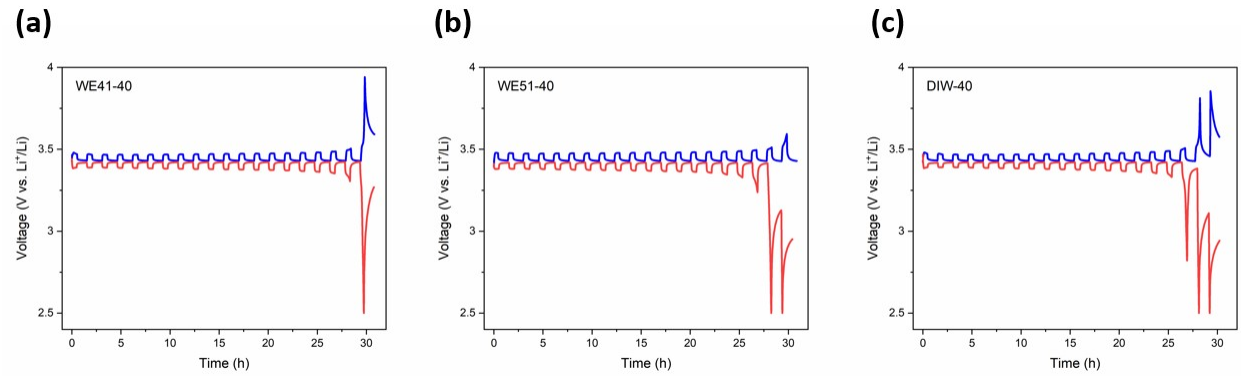

Fig. S13. GITT profile of (a) WE41-40, (b) WE51-40 and (c) DIW-40 electrodes.

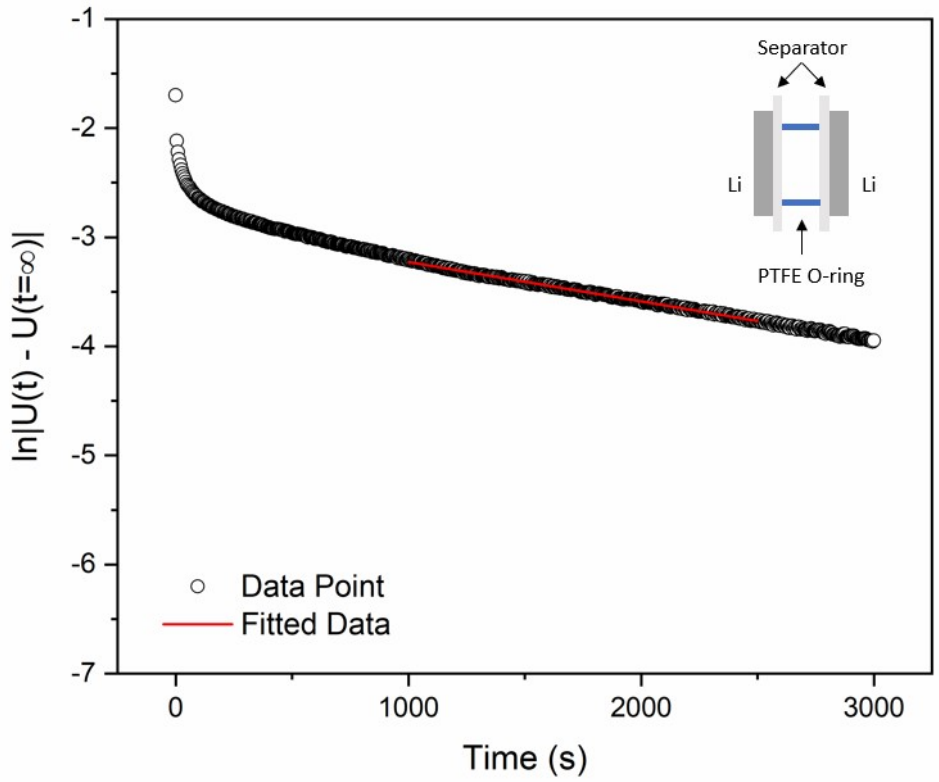

Fig. S14. Plot of ln|U(t) – U(t = ∞)| versus time for the measurement of diffusivity of electrolyte (1 M $LiPF_6$ in 3:7 mass ratio of EC: EMC) and fitted data of linear region. The inset shows the symmetric cell with PTFE O-ring as a spacer.

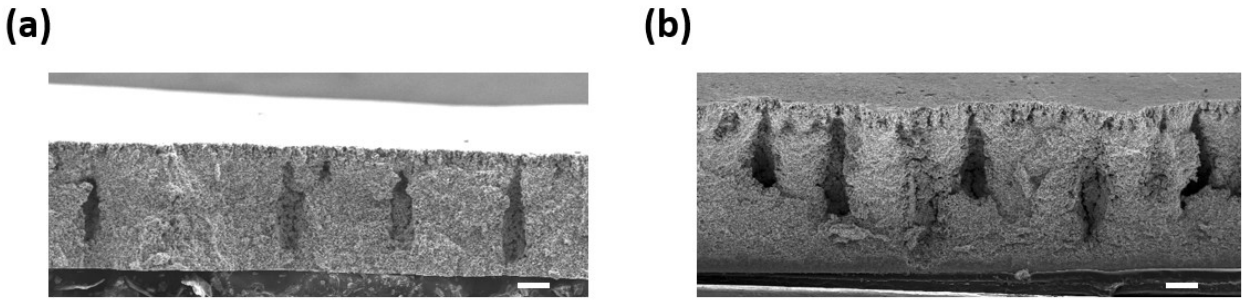

Fig. S15. SEM images of (a) WE31-20 and (b) WE31-30 electrodes (scale bar: 100 μm).

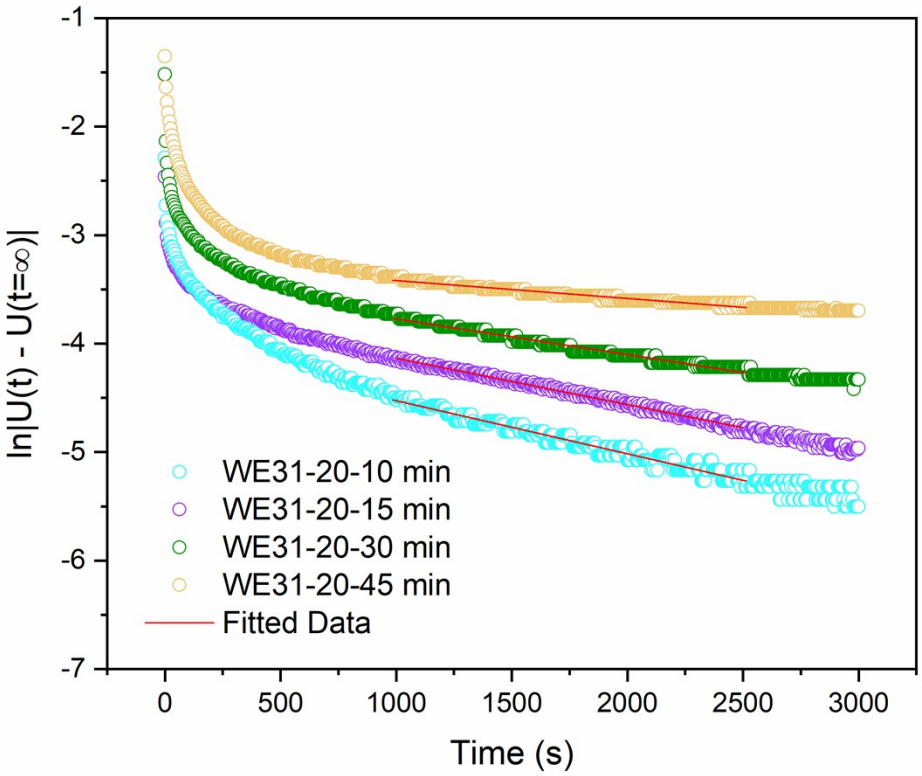

Fig. S16. Plots of $\ln|U(t) - U(t = \infty)|$ versus time for the electrodes with mass loading of 20 mg/cm^2 fabricated by various phase-inversion processing time in 3:1 water-to-ethanol ratio as non-solvent.

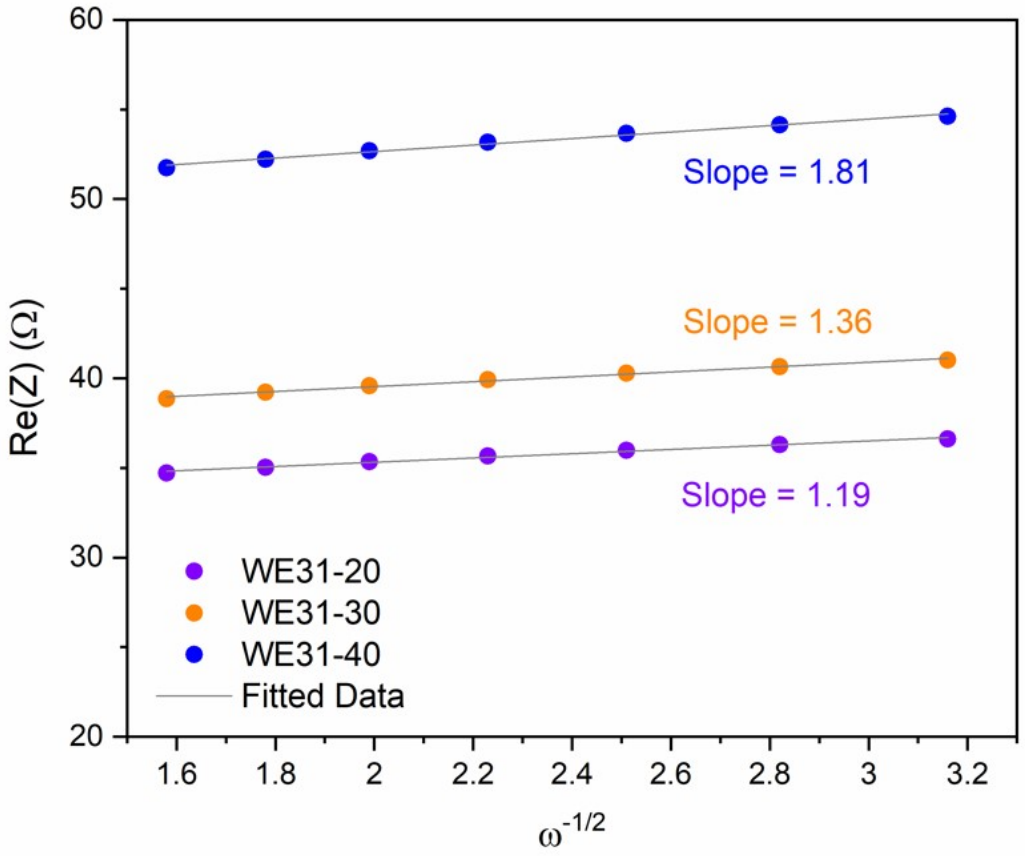

Fig. S17. Real impedance of low-frequency region from Nyquist plots of WE31-20, WE31-30 and WE31-40 electrodes and the fitted data of impedance vs. inverse square root of angular frequency ($\omega^{-1/2}$).

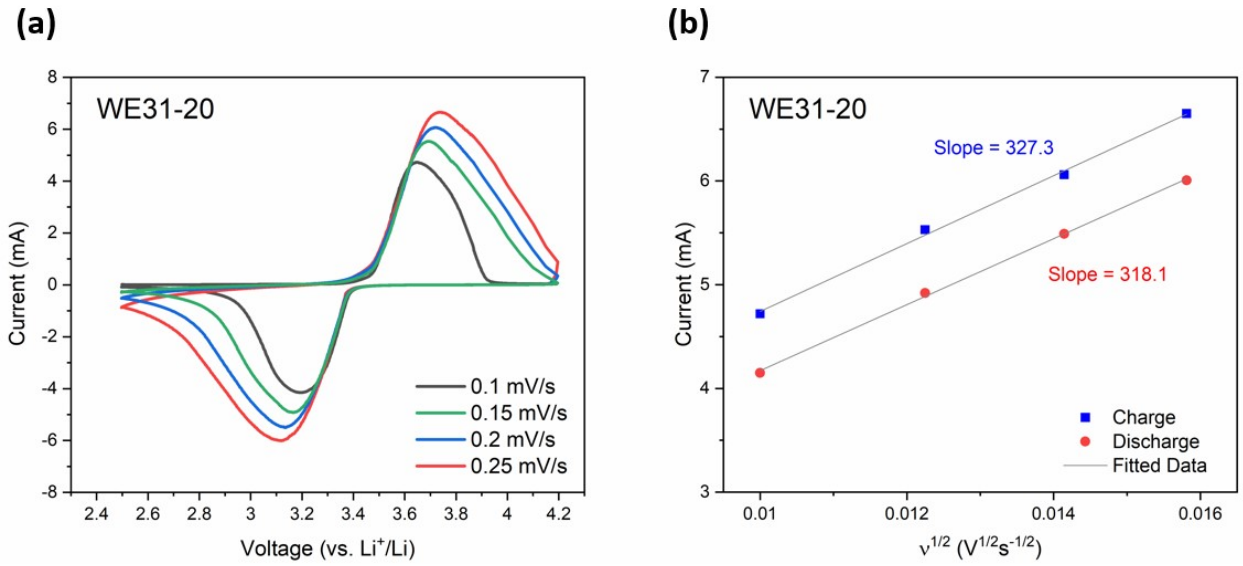

Fig. S18. (a) Cyclic voltammogram of WE31-20 electrode at scan rate of 0.1, 0.15, 0.2 and 0.25 mV/s; (b) Fitted data of peak current versus square root of scan rate in anodic and cathodic region for WE31-20 electrode.

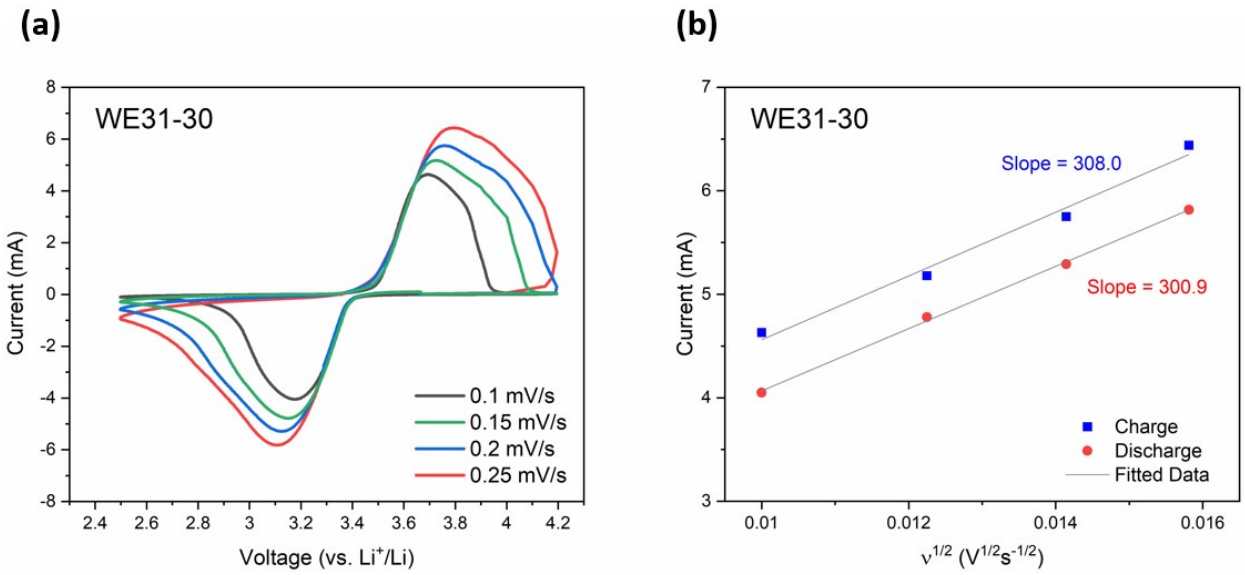

Fig. S19. (a) Cyclic voltammogram of WE31-30 electrode at scan rate of 0.1, 0.15, 0.2 and 0.25 mV/s; (b) Fitted data of peak current versus square root of scan rate in anodic and cathodic region for WE31-30 electrode.

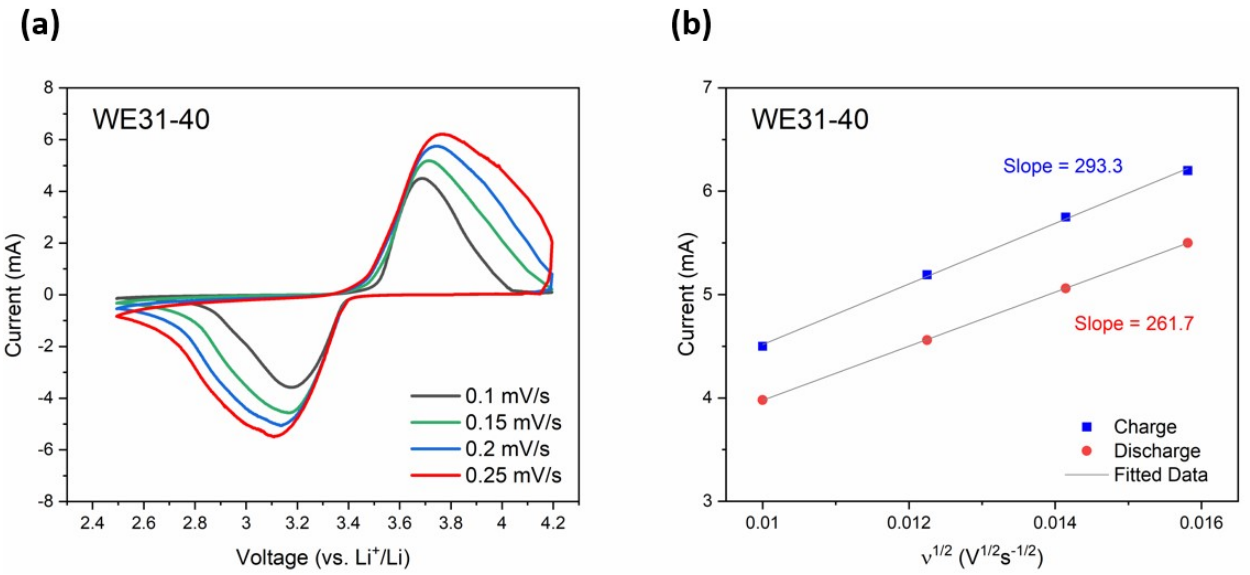

Fig. S20. (a) Cyclic voltammogram of WE31-40 electrode at scan rate of 0.1, 0.15, 0.2 and 0.25 mV/s; (b) Fitted data of peak current versus square root of scan rate in anodic and cathodic region for WE31-40 electrode.

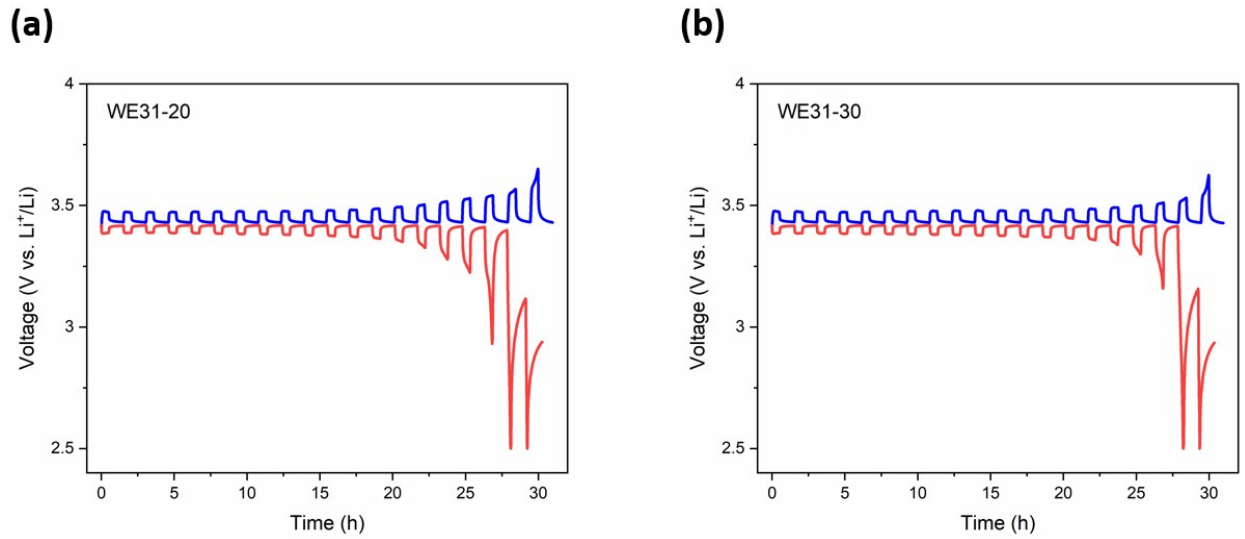

Fig. S21. GITT profiles of (a) WE31-20 and (b) WE31-30 electrodes.

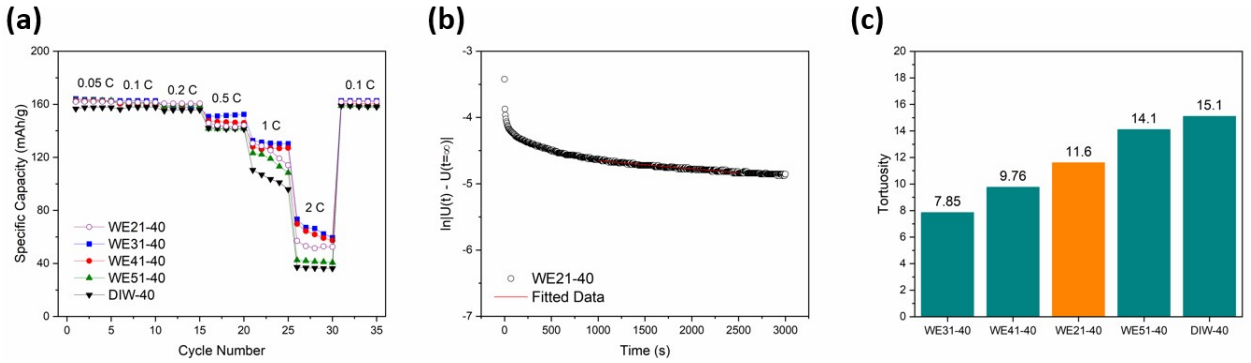

Fig. S22. (a) Rate performance comparison between WE21-40 electrode and four electrodes fabricated in non-solvent with higher water ratio during phase-inversion process. (b) Plot of ln|U(t) – U(t = ∞)| versus time for the WE21-40 electrode for measurement of effective diffusivity. (c) Comparison of tortuosity between WE21-40 electrode and four electrodes fabricated in non-solvent with higher water ratio during phase-inversion process.

Table S1. Specific discharge capacity (mAh/g) at each C-rate for all the electrodes.

Electrode	0.05 C	0.1 C	0.2 C	0.5 C	1 C	2 C
WE31-20	164.92	164.04	161.68	156.08	145.15	95.44
WE31-30	164.24	163.47	160.72	156.92	143.19	75.19
WE31-40	164.10	162.63	158.19	151.98	132.72	73.32
WE41-40	163.11	160.38	156.44	146.91	127.96	69.82
WE51-40	162.86	161.37	159.37	141.67	123.19	42.50
DIW-40	157.53	156.17	155.04	141.44	110.39	37.17

Table S2. Internal (R_u) and charge transfer (R_{ct}) resistance of each electrode and estimated lithium-ion diffusion from low-frequency region of Nyquist plots.

Electrode	R_u (Ω)	R_{ct} (Ω)	D_{Li^+} ($cm^2\ s^{-1}$)
WE31-20	6.18	31.1	1.55×10^{-8}
WE31-30	5.78	35.9	1.19×10^{-8}
WE31-40	6.99	52.9	6.70×10^{-9}
WE41-40	5.56	63.5	3.97×10^{-9}
WE51-40	7.23	71.3	3.74×10^{-9}
DIW-40	6.30	83.6	1.45×10^{-9}

Table S3. Slopes of fitted data of peak current versus square root of scan rate from cyclic voltammetry and estimated lithium-ion coefficients.

Electrode	Charge ($A\ s^{1/2}\ V^{-1/2}$)	D_{Li^+} ($cm^2\ s^{-1}$) (Charge)	Discharge ($A\ s^{1/2}\ V^{-1/2}$)	D_{Li^+} ($cm^2\ s^{-1}$) (Discharge)
WE31-20	0.327	1.76×10^{-9}	0.318	1.66×10^{-9}
WE31-30	0.308	1.56×10^{-9}	0.301	1.49×10^{-9}
WE31-40	0.293	1.41×10^{-9}	0.261	1.12×10^{-9}
WE41-40	0.284	1.33×10^{-9}	0.238	9.32×10^{-10}
WE51-40	0.194	6.19×10^{-10}	0.154	3.90×10^{-10}
DIW-40	0.176	5.10×10^{-10}	0.077	9.76×10^{-11}

Table S4. Calculated lithium-ion diffusion coefficients from GITT measurements.

Electrode	D_{Li^+} **(cm^2 s^{-1})**
WE31-20	1.50×10^{-9}
WE31-30	1.18×10^{-9}
WE31-40	4.90×10^{-10}
WE41-40	4.36×10^{-10}
WE51-40	2.97×10^{-10}
DIW-40	1.30×10^{-10}

Table S5. Measured effective diffusivity, tortuosity, and porosity of each electrode.

Electrode	Thickness (μm)	Porosity	Effective Diffusivity ($cm^2\ s^{-1}$)	Tortuosity
WE31-20	450	69.2%	8.91×10^{-8}	7.44
WE31-30	650	68.0%	8.53×10^{-8}	7.64
WE31-40	846	67.2%	8.21×10^{-8}	7.85
WE41-40	845	67.2%	6.60×10^{-8}	9.76
WE51-40	849	67.3%	4.59×10^{-8}	14.1
DIW-40	855	67.5%	4.23×10^{-8}	15.1

Table S6. Effective diffusivity and estimated tortuosity of each WE31-20 electrode processed for different time in phase-inversion

Electrode	Thickness (µm)	Porosity	Effective Diffusivity ($cm^2\ s^{-1}$)	Tortuosity
WE31-20-10min	455	69.5%	9.98×10^{-8}	6.68
WE31-20-15min	450	69.2%	8.91×10^{-8}	7.44
WE31-20-30min	443	68.7%	6.72×10^{-8}	9.80
WE31-20-45min	440	68.5%	3.92×10^{-8}	16.7

References

1 M. Romay, N. Diban and A. Urtiaga, *Polymers*, 2021, **13**, 678.

2 Y. M. Wei, Z. L. Xu, X. T. Yang and H. L. Liu, *Desalination*, 2006, **192**, 91–104.

3 F. W. Altena and C. A. Smolders, *Macromolecules*, 1982, **15**, 1491–1497.

4 C. Özdemir and A. Güner, *Eur. Polym. J.*, 2007, **43**, 3068–3093.

5 J. Y. Lai, S. F. Lin, F. C. Lin and D. M. Wang, *J. Polym. Sci. B Polym. Phys.*, 1998, **36**, 607–615.

6 G. R. Guillen, Y. Pan, M. Li and E. M. V. Hoek, *Ind. Eng. Chem. Res.*, 2011, **50**, 3798–3817.

7 A. C. Lazanas and M. I. Prodromidis, *ACS Meas. Sci. Au*, 2023, 3, 162–193.

8 W. Weppner and R. A. Huggins, *J. Electrochem. Soc.*, 1977, **124**, 1569.

9 P. Zanello and N. G. Connelly, *Inorganic electrochemistry: Theory, practice and application*, Royal Society of Chemistry, 2003, ch. 3, pp. 49-136.

10 J. Maier, *Physical chemistry of ionic materials: Ions and Electrons in Solids*, John Wiley & Sons, 2004, ch. 7, pp. 399-499.